JYX
JYVÄSKYLÄN YLIOPISTO
UNIVERSITY OF JYVÄSKYLÄ

This is a self-archived version of an original article. This version may differ from the original in pagination and typographic details.

Author(s): Mattelaer, Felix; Van Daele, Michiel; Minjauw, Matthias M.; Nisula, Mikko; Elliott, Simon D.; Sajavaara, Timo; Dendooven, Jolien; Detavernier, Christophe

Title: Atomic layer deposition of localised boron- and hydrogen-doped aluminium oxide using trimethyl borate as a dopant precursor

Year: 2020

Version: Accepted version (Final draft)

Copyright: © 2019 American Chemical Society

Rights: In Copyright

Rights url: http://rightsstatements.org/page/InC/1.0/?language=en

Please cite the original version:

Mattelaer, F., Van Daele, M., Minjauw, M. M., Nisula, M., Elliott, S. D., Sajavaara, T., Dendooven, J., & Detavernier, C. (2020). Atomic layer deposition of localised boron- and hydrogen-doped aluminium oxide using trimethyl borate as a dopant precursor. Chemistry of Materials, 32(10), 4152-4165. https://doi.org/10.1021/acs.chemmater.9b04967

CHEMISTRY OF MATERIALS

Subscriber access provided by JYVASKYLAN UNIV

Article

Atomic layer deposition of localised boron- and hydrogen-doped aluminium oxide using trimethyl borate as a dopant precursor

Felix Mattelaer, Michiel Van Daele, Matthias M. Minjauw, Mikko Nisula, Simon D. Elliott, Timo Sajavaara, Jolien Dendooven, and Christophe Detavernier

Chem. Mater., **Just Accepted Manuscript** • DOI: 10.1021/acs.chemmater.9b04967 • Publication Date (Web): 23 Apr 2020

Downloaded from pubs.acs.org on April 26, 2020

Just Accepted

"Just Accepted" manuscripts have been peer-reviewed and accepted for publication. They are posted online prior to technical editing, formatting for publication and author proofing. The American Chemical Society provides "Just Accepted" as a service to the research community to expedite the dissemination of scientific material as soon as possible after acceptance. "Just Accepted" manuscripts appear in full in PDF format accompanied by an HTML abstract. "Just Accepted" manuscripts have been fully peer reviewed, but should not be considered the official version of record. They are citable by the Digital Object Identifier (DOI®). "Just Accepted" is an optional service offered to authors. Therefore, the "Just Accepted" Web site may not include all articles that will be published in the journal. After a manuscript is technically edited and formatted, it will be removed from the "Just Accepted" Web site and published as an ASAP article. Note that technical editing may introduce minor changes to the manuscript text and/or graphics which could affect content, and all legal disclaimers and ethical guidelines that apply to the journal pertain. ACS cannot be held responsible for errors or consequences arising from the use of information contained in these "Just Accepted" manuscripts.

is published by the American Chemical Society. 1155 Sixteenth Street N.W., Washington, DC 20036
Published by American Chemical Society. Copyright © American Chemical Society. However, no copyright claim is made to original U.S. Government works, or works produced by employees of any Commonwealth realm Crown government in the course of their duties.

1
2
3
4
5
6
7
8
9
10
11
12
13
14
15
16
17
18
19
20
21
22
23
24
25
26
27
28
29
30
31
32
33
34
35
36
37
38
39
40
41
42
43
44
45
46
47
48
49
50
51
52
53
54
55
56
57
58
59
60

Atomic layer deposition of localised boron- and hydrogen-doped aluminium oxide using trimethyl borate as a dopant precursor

Felix Mattelaer,[*,†] Michiel Van Daele,[†] Matthias M. Minjauw,[†] Mikko Nisula,[†] Simon D. Elliott,[‡] Timo Sajavaara,[¶] Jolien Dendooven,[†] and Christophe Detavernier[†]

†*Department of Solid State Sciences, Ghent University, Krijgslaan 281 S1, 9000 Gent, Belgium*

‡*Schrödinger Inc., 120 West 45th Street, 17th Floor, New York, NY 10036-4041, USA*

¶*Department of Physics, University of Jyväskylä, P.O. Box 35, FI-40014 Jyväskylä, Finland*

E-mail: felix.mattelaer@ugent.be

Abstract

Atomic layer deposition (ALD) of boron-containing films has been mainly studied for use in 2D materials and for B-doping of Si. Furthermore, lithium-containing borates show great promise as solid electrolyte coatings for enhanced energy storage. In this work, we examine trimethyl borate (TMB) in combination with O_2 plasma as precursors for ALD of B-containing films, targeting the growth of B_2O_3. It is found that after initial growth on a SiO_2 or Al_2O_3 surface, a rapid decrease of the growth rate during subsequent ALD cycles occurs indicating surface inhibition during continued growth. DFT cluster calculations in combination with in-situ FTIR demonstrated

that the growth is governed by two different mechanism depending on the Lewis acidity of the surface: chemisorption on Al-OH and Si-OH terminated surface and physisorption on more acidic B-OH surface sites. The growth could be maintained in a mixed process, by re-activating the surface through single exposures to trimethyl aluminum (TMA) and oxygen plasma and thus resetting the surface to Al-OH, on which TMB chemisorption is energetically more favourable. Surprisingly, this process did not result in B_2O_3 (or Al-doped B_2O_3) films, but instead in B- and H-doped Al_2O_3 films. Moreover, rather than uniform boron distribution, the Al_2O_3 films grown from this process contain a large amount of hydrogen, up to 17 At% under certain processing conditions, and displayed non-uniform depth distributions of boron and hydrogen with a degree of control over the doping distribution based on the deposition conditions. Finally, the mechanism for the atypical growth mode is proposed based on in-situ FTIR and ellipsometry measurements and density functional theory calculations, and was attributed to sub-surface reactions of the TMA with the B-OH films grown by TMB-O_2 plasma. This makes the process an interesting, albeit atypical, ALD process that allows for a quasi-continuous tuning of the B-concentration in the top region of high-purity Al_2O_3 films.

Introduction

Boron finds one of its main applications on a thin film level in semiconductors, where it is used commonly as a dopant to induce p-type conductivity in silicon. However, emerging thin-film applications, such as 2D-materials (e.g. h-BN[1–3]) and thin-film electrolytes (e.g. lithium borophosphates[4–7] or borocarbonates[8–12]) have renewed interest in the controlled deposition of B-containing films. Especially for the latter applications, atomic layer deposition (ALD) of these materials can potentially prove ground breaking thanks to its uniform and pinhole-free films, and especially given the almost unrivalled conformality, making it an indispensable technique for both microelectronics, where it is well established, as well as for

1
2
3
4
5
6
7
8
9
10
11
12
13
14
15
16
17
18
19
20
21
22
23
24
25
26
27
28
29
30
31
32
33
34
35
36
37
38
39
40
41
42
43
44
45
46
47
48
49
50
51
52
53
54
55
56
57
58
59
60

emerging applications such as catalysis and energy storage.[13–16]

For the deposition of multicomponent materials with ALD, a typical method is to use the so-called sub-cycle approach, in which the appropriate binary processes are used as the build blocks.[17] By changing the cycle ratio, it is in principle possible to accurately tune the stoichiometry of the target material. However, the surface chemistry of each of the constituent binary processes can influence the others, and it becomes imperative to fully understand the underlying reaction mechanisms for accurate process control. In this work, by using various in-situ and ex-situ techniques, we reveal that the case of boron is especially intriguing considering both binary and mixed processes.

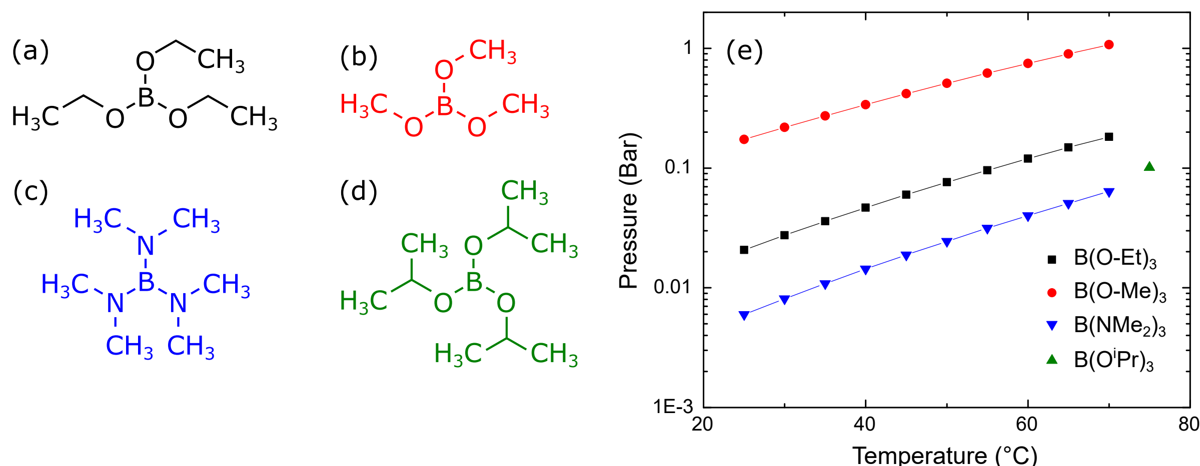

Figure 1: Graphical representation of some selected boron precursors: (a) $B(O{-}Et)_3$, (b) $B(O{-}Me)_3$, (c) $B(NEtMe)_3$ and (d) $B(O^iPr)_3$. (e) The reported vapour pressures at various precursor pressures, as reported by Christopher and Shilman[42].

Considering the commercially available and investigated boron precursors for ALD, summarised in table 1, trimethyl borate ($B(OMe)_3$, hereafter TMB) (see Figure 1(a) and (b)) was selected as the precursor for this work based on two arguments. On the one hand, it is a liquid at room temperature with a high vapour pressure, as is clear from Figure 1(e). TMB exhibits vapour pressure of 0.22 bar at room temperature.[42] This lowers risks of condensation and enables use without any source heating, as is the case for $B(NMe_2)_3$ (source temperature 60 °C)[36–38] and the precursors for direct deposition of metal borates, such as

Table 1: Overview of reported boron precursors used in atomic layer deposition.

B-precursor	Co-reagent	Deposited films	Temperature	
B_2H_6	DEZ and H_2O	B-doped ZnO	150 °C	[18,19]
BCl_3	NH_3	BN	227 °C	[20–23]
BBr_3	NH_3	BN	250 °C to 750 °C	[24–27]
	H_2O	B_2O_3	20 °C to 50 °C	[28]
$Ba(Tp^{Et2})_2$ [a]	H_2O	BaB_2O_4	250 °C to 375 °C	[29]
$CaTp_2$ [b]	H_2O	CaB_2O_4	300 °C to 375 °C	[30]
$SrTp_2$ [b]	H_2O	SrB_2O_4	300 °C to 375 °C	[31]
$B(O{-}Et)_3$ [c]	WF_6 and NH_3	WN_xC_y	300 °C to 350 °C	[32–34]
$B(O{-}Me)_3$ [d]	(H_2O), O_3, O_2^*	B_2O_3	150 °C	[35]
$B(NMe_2)_3$ [e]	O_3, O_2^*	B_2O_3	20 °C to 100 °C	[36–38]
$B(O^iPr)_3$ [f]	DEZn and H_2O	B-doped ZnO	150 °C	[39]
	$Li(O^tBu)$ and O_3	Li_3BO_3–Li_2CO_3	200 °C to 260 °C	[12]
TCB [g]	HMDS [h]	BN	80 °C to 150 °C	[40]
$B(NEtMe)_3$ [i]	NH_3^*	h-BN	250 °C to 350 °C	[2]
$B_3N_3H_6$	e^-	h-BN	20 °C to 100 °C	[3]
B_2F_4	H_2O	B_2O_3	300 °C	[41]

[a] Tp^{Et2} = tris(3,5-diethylpyrazolyl)borate
[b] Tp = tris(pyrazolyl)borate
[c] Et = ethyl
[d] Me = methyl
[*] plasma
[e] NMe_2 = dimethylamido
[f] O^iPr = isopropyl
[g] TCB = trichloroborazine
[h] HMDS = hexamethyldisilazane
[i] NEtMe = ethylmethylamino

$Ba(Tp^{Et2})_2$ (source temperature 205 °C).[29] The high vapour pressure is also promising for use in atmospheric-pressure ALD systems. Furthermore, TMB poses more limited safety risks compared to other precursors listed in table 1. While TMB is flammable and burns with a bright green flame, it is not pyrophoric (as B_2H_6) and less toxic than BCl_3 and BBr_3.

Borate esters have been evaluated for CVD in earlier work, for example for the deposition of borophosphosilicate glass.[43] Already in 2003, the group of Suvi Haukka and Marko Tuominen evaluated the use of triethyl borate in an ALD process, targetting the incorporation of carbon in WN_xC_y films using WF_6 and NH_3 as tungsten and nitrogen sources, respectively.[32–34] More than 10 years later, TMB was tested by Kim et al for the ALD of B_2O_3, to obtain mixed B_2O_3/SiO_2 films.[35] In that work, both ozone and oxygen plasma proved effective combustion agents for the methyl ligands at a temperature of 150 °C. In this work, we investigate the surface chemistry of TMB in combination with O_2 plasma as co-reagent for the deposition of films in an ALD-like fashion, both in a binary process (to deposit B_2O_3) and in a mixed film growth in combination with ALD of Al_2O_3 using trimethyl aluminum (TMA) and oxygen plasma as precursors. It is found out that the reaction mechanism is dependent on the Lewis acidity of the surface resulting in two different growth modes: chemisorption on Al-OH and Si-OH terminated surface and physisorption on more acidic B-OH surface sites. In the mixed growth mode with TMA, a non-linear depth distribution of boron and hydrogen is found. Moreover, the depth profile can be controlled by adjusting the ratio of the subcycles. As a side product, the B_2O_3 process appears to 'clean' the underlying alumina layer of hydrogen impurities.

Experimental

The ALD films were deposited in a home-built high-vacuum ALD reactor[44–46] with a base pressure of 10^{-7} mbar. The reactor walls were heated to 95 °C to avoid precursor condensa-

tion. Trimethyl aluminium (TMA) and O_2 plasma were used to deposit amorphous Al_2O_3, and trimethyl borate (TMB) was used with O_2 plasma for the deposition of the boron-containing films. All precursors were obtained from Sigma Aldrich, and the O_2 gas used to generate O_2 plasma was obtained from Air Liquide (99.999 %). TMA and TMB were used at room temperature. The plasma was generated in a fused-quartz column wrapped in a copper coil, connected to a 13.56 MHz RF plasma generator and a matching network, resulting in an inductively coupled RF plasma of 300 W at a pressure of 1×10^{-2} mbar. Precursor pulses of 5×10^{-3} mbar were alternated with pump times allowing the pressure to drop to 10^{-6} mbar. Films were deposited on thermal SiO_2 on Si substrates to monitor the thickness.

Film thickness was determined post-deposition using X-ray reflectivity (XRR) on a Bruker D8 diffractometer using Cu Kα radiation. Cross-sectional scanning electron microscopy (cross-SEM) was used to estimate film thickness on films that were not suited for X-ray reflectivity, using a FEI Quanta 200F high-vacuum electron microscope. Film thickness was characterised *in-situ* by spectroscopic ellipsometry (SE). The deposited film thickness was obtained from fitting recorded data using a Cauchy model in the CompleteEase software package, resulting in a good match of the thickness to the XRR-measured values, which was performed where possible. The ellipsometer used was a J.A. Woollam M-2000 with a wavelength range of 245 nm to 1000 nm.

Film composition was examined using X-ray photoelectron spectroscopy (XPS) and time-of-flight elastic recoil detection (ToF-ERD). XPS was performed on a Thermo Scientific Theta Probe tool using Al Kα radiation (15 kV, 70 W) on a 0.3 mm diameter spot focussed by a MXR1 monochromator. XPS depth profiling was performed by etching the sample using Ar^+-ions (3 keV, 2 µA). ToF-ERD was performed using a home-built spectrometer using a 1.7 MV Pelletron accelerator in Jyväskylä.[47] The incident particle beam for these measurements consisted of 11.915 MeV $^{63}Cu^{7+}$ ions at an incoming angle of 10° and a measuring

angle of 31°, equalling a total scattering angle of 41°. The collected spectra were analysed using in-house developed open-source software called Potku.[48]

In-situ infrared spectroscopy during the deposition process was performed on an FTIR spectrometer (Bruker, Model VERTEX 70 V) with KBr beamsplitter and a liquid nitrogen-cooled MCT detector (mid-infrared). The measurements were done in reflection mode, and a silicon wafer with a 60 nm TiN film, which was overcoated with 100 cycles ALD Al_2O_3 (TMA - O_2 plasma) . The metallic TiN film acted as an FTIR mirror and the ALD Al_2O_3 acted as the nucleation layer for the surface reactions of interest and also shielded the reflective TiN layer.

Cluster models have frequently been used for density functional theory (DFT) calculations of the structure and bonding of precursors during ALD reactions, including TMA.[49] When compared with more sophisticated periodic surface models,[50] the cluster models yield adequate accuracy in reaction energetics (but not kinetics) in a fraction of the computational time. Cluster models are therefore employed here to examine the trends in adsorption of the TMB, TEB and TMA precursors onto hydroxylated borate and alumina surfaces, modelled as $B(OH)_3$ and $Al(OH)_3$ molecules respectively. As our interest is in relative bond strength, we focus on the differences in electronic energy at T=0 K, rather than estimating free energy changes. Clusters were computed at the DFT level using the Jaguar code.[51] Electronic structure was computed using the hybrid B3LYP functional[52,53] with D3 dispersion corrections[54,55] and LAV3P** basis set with an effective core potential on Al,[56,57] converged in each step to energy differences $< 5\times10^{-5}$ E_{H} and RMS density matrix differences $< 5\times10^{-6}$. Molecular structures were optimized freely using redundant internal coordinates until energy changes were $< 5\times10^{-5}$ E_{H} and RMS gradient changes were $< 3\times10^{-4}$ atomic units. Computed structures and key reaction energies are provided in the Supplementary Information.

1
2
3
4
5
6
7
8
9
10
11
12
13
14
15
16
17
18
19
20
21
22
23
24
25
26
27
28
29
30
31
32
33
34
35
36
37
38
39
40
41
42
43
44
45
46
47
48
49
50
51
52
53
54
55
56
57
58
59
60

Results And Discussion

ALD growth characteristics of TMB

In this work, TMB was investigated in-depth for the deposition of boron oxide using PE-ALD with oxygen plasma, and combined with a PE-ALD process for Al_2O_3 to overcome growth inhibition likely related to surface passivation observed during the TMB processes.

Similar to the work of Kim et al.[35], it was observed that the boron oxide films were sensitive to ambient air, and in particular the water in the ambient, causing film degradation and decrease in the film thickness. This is likely due to reaction of the B_2O_3 with ambient humidity and subsequent formation of boric acid, $B(OH)_3$. The thickness decrease is then due to the volatility of $B(OH)_3$ This indicates that great care needs to be taken when depositing these films for post-deposition analysis or processing, and in this work all samples for ex-situ characterization were capped with a 5 nm Al_2O_3 film grown from TMA and O_2 plasma to avoid direct air exposure.

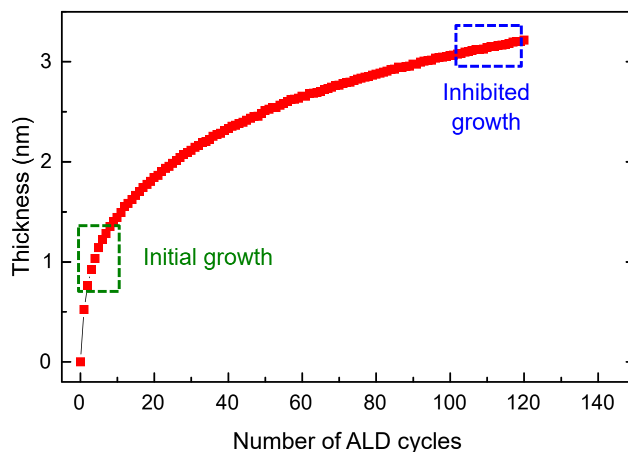

Figure 2: Growth characteristics collected using in-situ ellipsometry on a silicon substrate at 100 °C, using 10 second pulses for both the TMB and O_2 plasma pulses. This clearly demonstrates *initial* and *inhibited* growth regimes.

1 2 3 4 5 6 7 8 9 10 11 12 13 14 15 16 17 18 19 20 21 22 23 24 25 26 27 28 29 30 31 32 33 34 35 36 37 38 39 40 41 42 43 44 45 46 47 48 49 50 51 52 53 54 55 56 57 58 59 60

Growth inhibition of the TMB - O_2 plasma process

For the TMB-O_2 plasma process, a decreasing growth rate was observed during the ALD experiment in contrast with linear growth obtained in earlier work on TMB by Kim *et al.*[35] On the other hand, similar decay of growth was reported by Mane *et al.*[41] with B_2F_4 as the boron precursor. Additionally, in contrary to these previous results, no growth was observed when H_2O was used as the co-reactant. In the growth curve of the plasma process in Figure 2 it is clear that a continuous decrease in growth per cycle (GPC) occurs with number of cycles, continuing until almost no growth is observed despite the pulsing of precursors. To examine this, in-situ FTIR was used during *initial*-stage ALD and *inhibited*-stage growth modes. To prevent any interaction with the TiN substrate, the surface was first passivated with an ALD Al_2O_3 film. The FTIR difference spectra in Figure 3 reveal the changes in surface chemistry, where upwards features indicate added components, and downwards features indicate the breaking of certain bonds. Figure 3(a) shows these difference spectra after precursor and after co-reagent pulses, revealing how each ALD half-cycle changes the film surface chemistry, while Figure 3(b) shows the sum of the components in Figure 3(a), showing what changes in the sample structure as a whole after each complete ALD cycle.

During the first TMB pulse, Al-bound OH groups are consumed to chemisorb the TMB molecule to the surface, as indicated from the small feature around $3750\,cm^{-1}$,[58–60] as shown in Figure 4. This is corroborated by the favourable adsorption of the TMB molecule onto hydroxylated alumina that is computed with DFT (Table S1, Supplementary Information), albeit about half as strong as that computed for TMA on the same surface (Table S3). The addition of a (partial) TMB molecule is further supported by CH-stretch signatures, originating from $O-CH_3$ and $O-CH_2$ signatures at $2960\,cm^{-1}$ and $2870\,cm^{-1}$, respectively,[60,61] a C-O bond stretching mode around $1100\,cm^{-1}$,[61] and a multi-featured signature of B−O stretching modes between $1250\,cm^{-1}$ and $1600\,cm^{-1}$.[60,61]

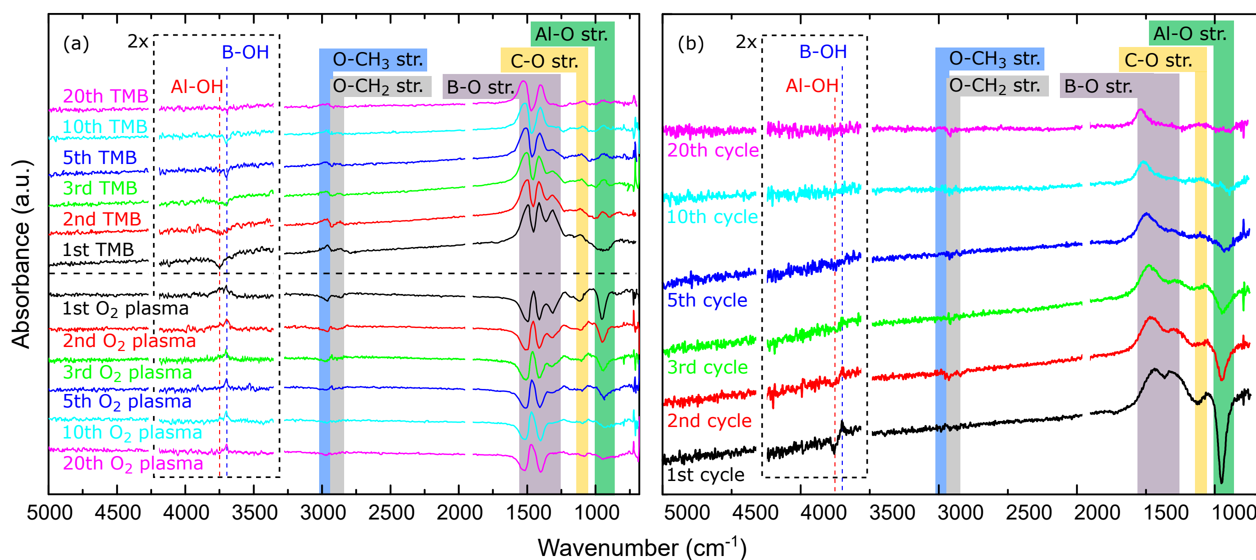

Figure 3: FTIR difference spectra after (a) ALD subcycles and (b) complete ALD cycles, recorded between $680\,cm^{-1}$ and $5000\,cm^{-1}$ during *initial* ALD growth using TMB and O_2 plasma on an Al_2O_3 surface at 100 °C.

The possibility of TMB physisorption without any chemical reaction can be excluded here due to the clear consumption of Al-bound OH groups. This points towards donation of protons from the OH groups to methoxide ligands of adsorbed TMB and elimination of methanol, CH_3OH, in a Brønsted acid-base reaction that is typical of ALD. Elimination of CH_4 from methoxide is not considered since it would require a reducing agent. This reaction mechanism is depicted in Figure 4. The DFT cluster calculations confirm that methoxide ligands are weak Brønsted bases. Based on previous calculations of the weak basicity of alkoxide ligands on Ti,[62] we expect that just a small proportion of the ligands will react in this way, subject to thermal activation, and that some of the methanol by-product may remain adsorbed at the surface until the co-reagent pulse (either by hydrogen bonding to the surface OH, by dative bonding to the boron centre, or both) as depicted in Figure 4. This is corroborated by the positive Al−OH feature during the plasma pulse, as the Al−OH sites shielded by the adsorbed methanol are freed up, causing this feature to re-appear as is evident from the broadness of the peak in the hydroxyl region of Figure 3(a) during the first plasma pulse.

During the O_2 plasma pulse, the ligands are combusted, as indicated by removal of the C-H streching modes asrising from the O−CH_3 groups. Previous computational studies of O_2-plasma-based ALD of Al_2O_3 have led to the general observation that each combusted organic ligand leaves behind a surface-OH group.[63,64] We therefore suggest that residual methoxide ligands bound to B are oxidised by O_2-plasma to B−OH surface groups. This is further corroborated by the addition of B−OH surface groups in the FTIR spectrum in Figure 3, at 3705 cm^{-1}, just below those of the Al−OH surface groups. Other simulations in the literature also show that combustion delivers substantial thermal energy to the surface and desorbing molecules (4-8 eV per reactive O atom).

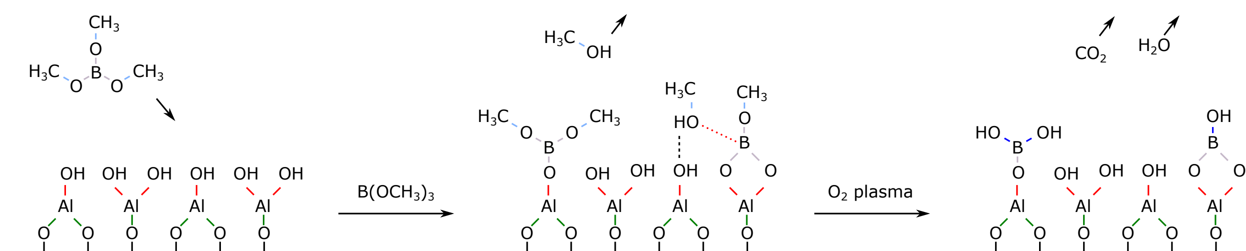

Figure 4: Hypothesised (sub)surface reactions during the *initial* growth of the TMB-O_2 plasma process on an Al_2O_3 surface. The bond colours are referring to the observed bonds in Figure 3. The black dashed line represent a hydrogen bond, while the red dotted line represents a dative bond.

In the initial stages of growth (cycles 1-2), it is clear that the B−O region is not symmetric when comparing the spectrum after the TMB pulse and after the O_2 plasma pulse in Figure 3(a), which is further clarified by the sum of these curves in Figure 3(b). Here, it is clear that B−O bonds are added to the films after one complete cycle, as well as Al-OH groups being removed and B-OH groups added. Furthermore, during the plasma pulse, there is reduction in intensity of the Al-O strecthing mode at 950 cm^{-1}, while a minor feature appears just above 1000 cm^{-1}. This could be related to the higher electronegativity of B (2.04) compared to that of Al (1.61). The formation of the B-O-Al bond reduces the electron density of O, thereby lowering the dipole moment and thus the absorption intensity

of the Al-O bond, explaining the observed changes. On top of that, the remaining Al-O signal will because of this dipole moment also be shifted to higher wavenumbers. This could potentially also explain the dual nature of the features in the B-O stretching region in Figure 3(b). The occurrence of a peak at low wavenumber (around $1300\,\mathrm{cm^{-1}}$) is only present as long as the negative feature of the Al-O stretch is present (below $1000\,\mathrm{cm^{-1}}$), indicating a relation between the two.

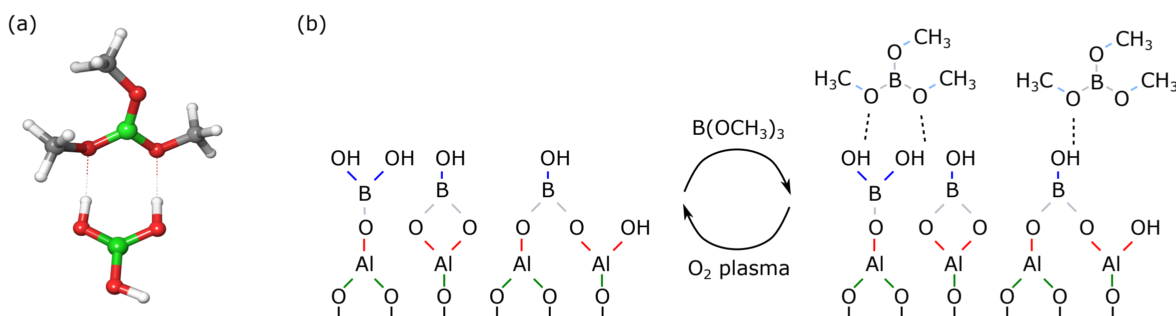

Figure 5: (a) Product structures of H-bonded TMB on $B(OH)_3$, representing the adsorption of TMB on a B-OH surface, as described in Table S1 (Supplementary Information). Green = B, red = O, grey = C, white = H. (b)Hypothesised surface reactions during the *inhibited*-growth mode of the TMB-O_2 plasma process on an Al_2O_3 surface. The dotted lines represent hydrogen bonding, which is shown to be more favourable on a $B(OH)_3$ surface. The bond colours are referring to the observed bonds in Figure 3. No net growth is depicted in this schematic.

From the FTIR in Figure 3(a) at higher cycle number, for example at cycle 20, it is clear that the TMB can still adsorb on the grown surface as is apparent from the many features in the B−O region. This region in the FTIR spectrum appears to be at almost the same intensity as for the initial cycle, indicating a similar amount of TMB adsorption on the surface. However, the adsorbed TMB is almost completely removed during the subsequent oxygen plasma pulse, as is clear from the cycle 20 spectrum in 3(b). The hypothesis is that during the growth of the initial layer, the surface is modified such that strong chemisorption of the TMB molecule no longer occurs. This hypothesis is corroborated by the hydroxyl region of Figure 3(a). During initial cycles, Al-bound OH-groups are consumed, chemisorbing the TMB molecules to the surface. However, cycle 10 and 20 show that no hydroxyl-removal

takes place during the TMB pulsing, indicating that the TMB may still adsorb on the surface but without the consumption of surface hydroxyl species, i.e. forming a weaker bond to the surface, and is almost completely removed again during the subsequent O_2 plasma pulse. This hypothesis is further confirmed by the DFT cluster calculations (Table S1, Supplementary Information), which show an energetic preference for H-bonding of TMB to a B-OH surface (Figure 5(a)), rather than forming new B-O-B bonds in Lewis acid-base chemistry. On the other hand, an Al-OH surface is computed to adsorb TMB either via H-bonds or as an Al-O-B Lewis adduct, with an energetic driving force favouring the latter. This demonstrates that a surface of sufficient Lewis basicity is required to chemisorb weakly-acidic B (via new bonds to surface O or OH) and ultimately allow deposition of B in the film. A similar explanation in terms of Lewis acidity has been given for the lack of ALD from $Ti(Cp\cdot)(OMe)_3$ and water (but not plasma).[62] These cluster calculations thus confirm why film growth is observed during *initial* growth on the Al-OH surface (TMB absorption as an Al-O-B Lewis adduct, Figure 4) and why the growth is *inhibited* on a B-OH surface (H-bonding of TMB to a B-OH surface, Figure 5). We therefore tentatively propose a two-phase mechanism for growth. In the initial growth phase is supported by TMB chemisorption on Al-OH surface sites leading to formation of an aluminum borate like surface layer. The inhibited growth phase is sustained by aforementioned physisorption of TMB. Upon the oxygen plasma exposure, the methyl ligands are combusted to form H_3BO_3-like surface layer. Boric acid is volatile under reduced pressure explaining the decreased growth rate.[65] On the other hand, at elevated temperatures it can also dehydrolyze leading to formation of the targeted B_2O_3 and densification of the surface layer.[66] The equilibrium between these two competing reactions is dependent on the process conditions such as pressure and temperature, thus explaining the observed differences in GPC between the present results and previous reports.

1
2
3
4
5
6
7
8
9
10
11
12
13
14
15
16
17
18
19
20
21
22
23
24
25
26
27
28
29
30
31
32
33
34
35
36
37
38
39
40
41
42
43
44
45
46
47
48
49
50
51
52
53
54
55
56
57
58
59
60

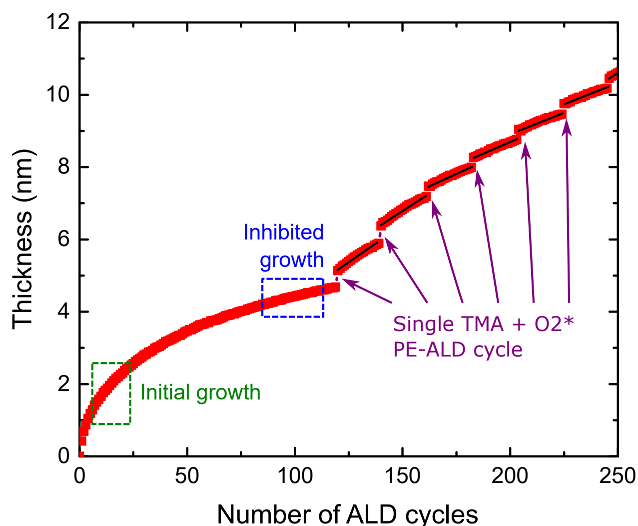

Figure 6: Growth characteristics collected using in-situ ellipsometry on a silicon substrate at 100 °C. The first 120 cycles consisted of a TMB pulse and an O_2 plasma pulse, showing the same '*initial*' and '*inhibited*' growth as in Figure 2. Cycle 121, 151, 171, ... are made up by a TMA pulse and O_2 plasma pulse, showing the '*reactivation*' of the surface, enabling the following 20 cycles of TMB and O_2 plasma to grow almost linearly. The black lines represent linear fits to these regimes used to make up the saturation curve in Figure 7.

Surface re-activation and ALD characteristics

To overcome this growth inhibition, following the work of Mane *et al.*[41] intermediate TMA-O_2 plasma pulses were introduced. As is clear from the FTIR in Figure 3 and the DFT calculations, the Al−OH surface is active towards chemisorption of the TMB molecule, so intermittent surface re-activation was attempted. Figure 6 shows the resulting growth behaviour. First, 120 cycles of subsequent pulses of TMB and oxygen plasma were performed. From this, it is clear that growth is slowing down dramatically, i.e. the deposited surface films are unfavourable for chemisorption of the TMB molecules, resulting in surface-inhibited growth. At the 121st cycle, the TMB is replaced by TMA, creating an ALD Al_2O_3 cycle. Here, an immediate increase in film thickness of about 0.4 nm is observed, which is much higher than that resulting from a single cycle of ALD Al_2O_3, suggesting sub-surface interaction of the TMA with the deposited film, as will be discussed in detail below. Remarkably, after this simple 'activation cycle', the subsequent TMB and O_2 plasma cycles exhibit an increased growth rate, resulting from the altered and more favourable surface chemistry. As

1
2
3
4
5
6
7
8
9
10
11
12
13
14
15
16
17
18
19
20
21
22
23
24
25
26
27
28
29
30
31
32
33
34
35
36
37
38
39
40
41
42
43
44
45
46
47
48
49
50
51
52
53
54
55
56
57
58
59
60

is clear from Figure 6, the first 20-30 cycles following the re-activation cycles are barely affected by the decreasing GPC observed during prolonged growth using only TMB and O_2 plasma.

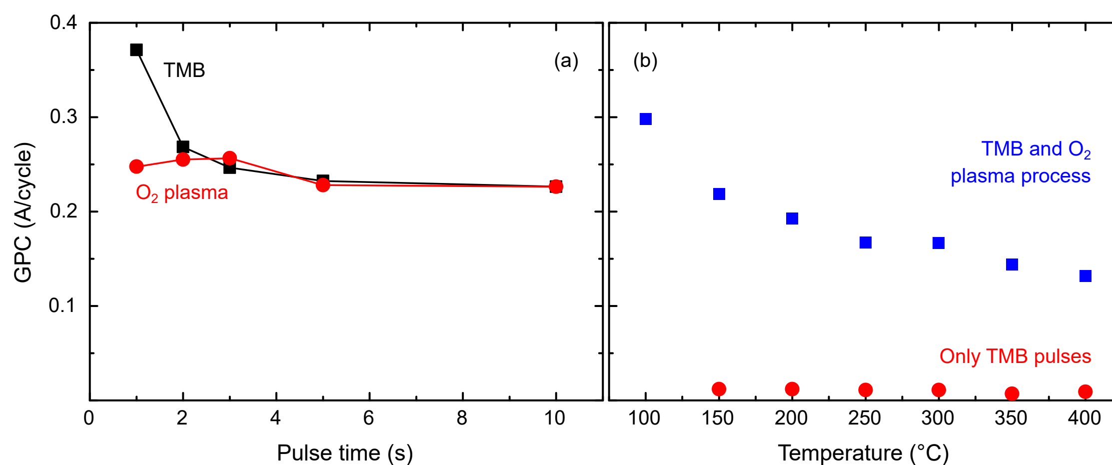

Figure 7: ALD characteristics as recorded by in-situ ellipsometry of the TMB and O_2 plasma process. Every reported GPC value is the result of 20 cycles under given conditions, following a TMA and O_2 plasma surface re-activation cycle. (a) saturation curves of the TMB and O_2 plasma pulses at 150 °C. (b) Growth rates at different temperatures for (red) TMB pulses without co-reagent pulse and (blue) subsequent pulses of TMB and O_2 plasma under saturated conditions according to (a).

While this process is clearly not a typical ALD process, as no linearity can be obtained due to the gradually decreasing GPC, the surface reactivation workaround still allows us to study other ALD characteristics of the TMB and O_2 plasma process, such as temperature window and saturation. Even in the absence of linearity in the overall process (see Figure 6 and the discussion above of the *initial*- and *inhibited*-growth regimes), saturation is clearly obtained in Figure 7(a), so for the remainder of this work we will label the " *TMA-reactivated* TMB and O_2 plasma process" an ALD process. Furthermore, in Figure 7(b) the intrinsic precursor stability of TMB is demonstrated by pulsing only TMB onto the reactivated surface for 20 times 20 seconds, which is much more than is required to saturate the TMB onto the surface. This was done to study precursor decomposition on the surface, which would be indicative of a parasitic CVD component in the process chemistry. Here, it is observed that

if no co-reagent step is introduced, chemisorption of TMB on the TMA-reactivated surface is self-saturating in a wide temperature window (100 °C to 300 °C).

This stability is in line with DFT results of an energy cost of 78.3 $kJ\,mol^{-1}$ for the beta-H-elimination of 1.5 C_2H_4 from one TMB molecule. If oxygen plasma is introduced as a co-reagent step, film growth is observed in the same temperature range. The growth rates are rather low, and decrease with increasing temperature: 0.30 Å/cycle at 100 °C down to 0.12 Å/cycle at 400 °C. This low growth rate and large degree of temperature sensitivity may again be linked to the H-bonding adsorption mode of TMB on the hydroxylated borate surface which, as described above, was found from DFT cluster calculations. These showed that TMB adsorption through H-bonding was energetically possible but not very strong. This implies that desorption of the entire molecule is always in competition with ligand elimination, and this could explain the low growth rate. Chemisorption and ligand elimination is computed to be substantially more favoured for TMA (Table S3, Supplementary Information), which leads to a GPC limited solely by steric hindrance to typically around 1 Å/cycle of Al_2O_3. Finally, dehydroxylation of an oxide surface at elevated temperature is well known and documented earlier for e.g. alumina and silica surfaces by Puurunen[67]. Dehydroxylation can explain the decreasing GPC with increasing temperature, due to the twin factors of less elimination of protonated ligands and weaker adsorption of TMB onto borate when H-bonding is not possible, as computed with DFT (Table S1, Supplementary Information).

Hydrogen- and boron-doped alumina

Mixed Al_2O_3-B_2O_3 PE-ALD growth

Because of the decreasing GPC, described above, this process could not be used to grow a pure boron oxide film. However, since surface reactivation induces semi-linear growth for a

1
2
3
4
5
6
7
8
9
10
11
12
13
14
15
16
17
18
19
20
21
22
23
24
25
26
27
28
29
30
31
32
33
34
35
36
37
38
39
40
41
42
43
44
45
46
47
48
49
50
51
52
53
54
55
56
57
58
59
60

Table 2: Overview of deposition condition of the intermixed samples. The TMA and TMB columns denote the number of cycles consisting of TMA or TMB as the metal source, where oxygen plasma was always used as co-reagent. All samples were also capped with 50 cycles of TMA and oxygen plasma to avoid water exposure.

	Supercycles	TMA	TMB	total cycle number
1:20	10	1	20	210
1:10	18	1	10	198
1:5	33	1	5	198
1:2	67	1	2	201
1:1	100	1	1	200

number of cycles, this process can be intermixed in supercycles with other ALD processes to form laminates or mixed oxides. Kim et al also used this ALD process to intermix SiO_2 and B_2O_3 films.[33,35] Here, as we used intermediate Al_2O_3 cycles to re-activate the TMB surface sticking, we studied the incorporation of boron in these alumina films. In order to do this the ratio of TMA and O_2 plasma ALD cycles to TMB and O_2 plasma ALD cycles (henceforth denoted as TMA:TMB) was varied from 1:1 to 1:20. Table 2 provides an overview of the cycle sequencing that was applied in this study. The total number of cycles was maintained as close to 200 cycles as possible to produce comparable samples. Finally, all samples were capped with a protective Al_2O_3 coating consisting of 50 cycles TMA and O_2 plasma. The deposition temperature was set to 100 °C according to the highest GPC obtained for the TMB/O_2 plasma process.

Elemental depth distributions

The resulting samples were examined using XPS depth profiling. Although XPS sensitivity for boron is quite low, the relative sensitivity is comparable to that of aluminum, rendering XPS a viable tool to qualitatively study the overall boron distribution in the films. To obtain a reliable quantitative B-concentration measurement, elastic recoil detection (ERD) is required, which will be discussed below in comparison to the XPS. Figure 8 shows the

1
2
3
4
5
6
7
8
9
10
11
12
13
14
15
16
17
18
19
20
21
22
23
24
25
26
27
28
29
30
31
32
33
34
35
36
37
38
39
40
41
42
43
44
45
46
47
48
49
50
51
52
53
54
55
56
57
58
59
60

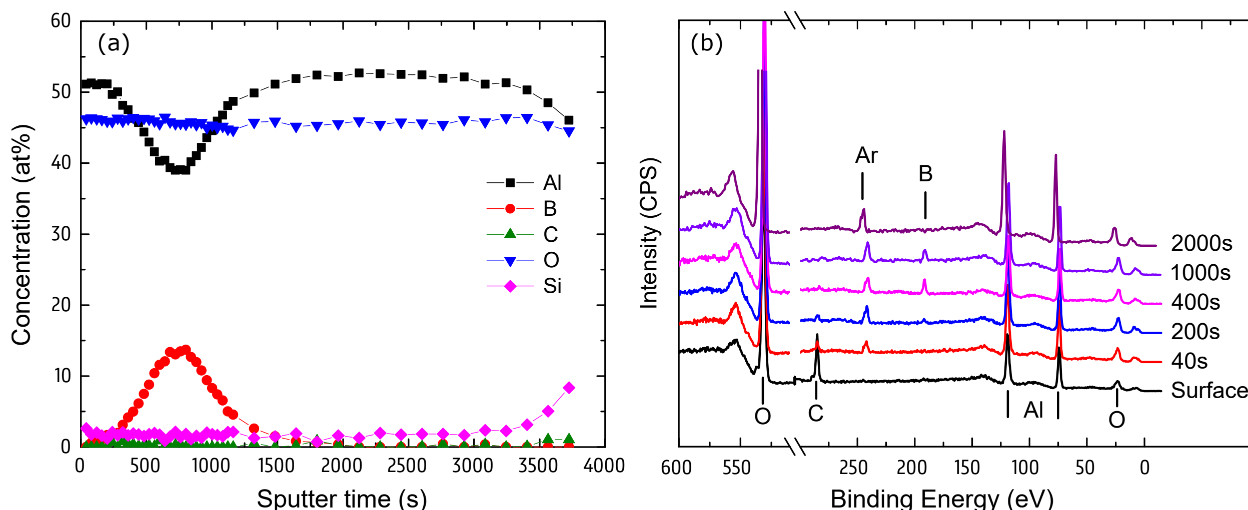

Figure 8: XPS (a) depth profile and (b) survey spectra at various depths in the 1:20 sample. The depth profiling steps were chosen with higher resolution near the surface to study the B-concentration, and with lower resolution near the silicon substrate to maintain reasonable measurement time.

depth distribution of the elements, obtained by gradually sputtering through the 1:20 deposited film and measuring detailed spectra at every depth level. The survey spectra shown in Figure 8(b) indeed show the presence of boron in the films, as evident from the peak at binding energies around 191 eV. Intermixing of ALD processes typically results in intimately intermixed ternary films. However, in this case that could not be further from the truth. Figure 8(a) shows the depth profile recorded. At low sputter times, i.e. near the surface of the films, a pure Al_2O_3 film is found as expected based on the intended deposition of Al_2O_3 as a protective capping layer. At sputtering times above 200 s, the Al content is decreased and at equal counts replaced by boron in the films, up to a maximum of 13 At% according to XPS. However, at sputtering depths above 800 s, the boron content decreases, and above 1500 s boron is below detection limit. The Gaussian shape of the boron distribution in the depth profile suggests that the boron is in an even narrower region than is revealed by the XPS depth profile. Below the boron-doped region, the film appears as a pure Al_2O_3 film until the silicon substrate is detected at sputter depths below 3500 s.

This anomalous behaviour is further strengthened if the other deposition conditions listed

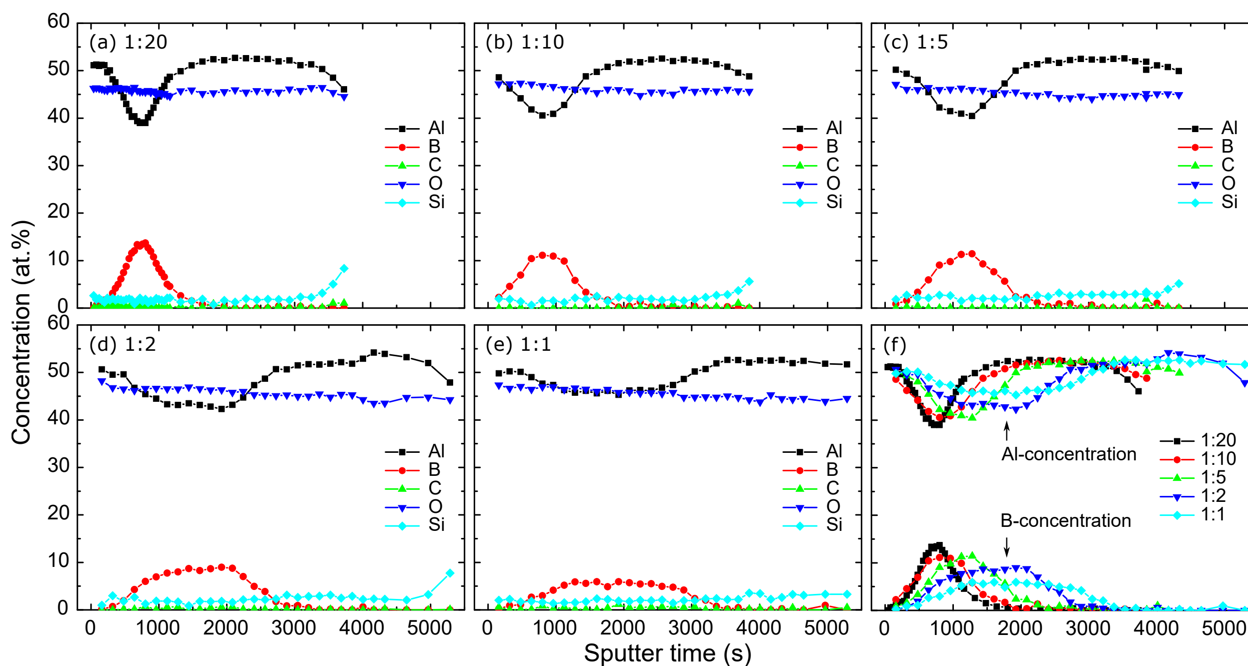

Figure 9: (a-e) XPS depth profiles of the samples deposited according to conditions listed in table 2: (a) 1:20, (b) 1:10, (c) 1:5, (d) 1:2 and (e) 1:1. (f) A comparison of the (top) aluminum- and (bottom) boron distributions between samples (a) through (e).

in table 2 are also examined, as shown in Figure 9(a) to (e). The 1:20 cycling ratio results in mainly boron doping at the surface up to 13 At% according to XPS, in a very narrow region near the surface. Lowering the TMB-based ALD cycle fraction from 1:20 to 1:1 effectively reduced the number of TMB-O_2 plasma cycles from 200 to 100. However, the amount of boron does not seem halved by this change, which will be further analysed by ERD. What is abundantly clear from XPS is that changing the cycling ratio changes the boron distribution to a more evenly distributed boron doped Al_2O_3 film. The 1:1 cycling ratio no longer results in a narrow doping region, but rather in a boron distribution of approximately 5 At% in the top half of the film. Interestingly, while the oxygen concentration remains constant throughout the films, the B-doped regions have a lower Al-concentration, as is clear from Figure 9(f). There is a clear exchange between boron and aluminum in the doping region.

1
2
3
4
5
6
7
8
9
10
11
12
13
14
15
16
17
18
19
20
21
22
23
24
25
26
27
28
29
30
31
32
33
34
35
36
37
38
39
40
41
42
43
44
45
46
47
48
49
50
51
52
53
54
55
56
57
58
59
60

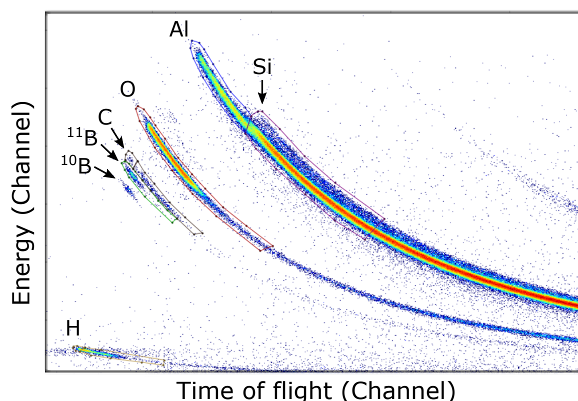

Figure 10: ERD spectrum of the 1:20 sample. Between so-called banana curves, more to the left-bottom corner of the plot (lower energy, lower t-o-f) means lower masses. Within a single banana shape, lower energy and higher t-o-f indicates elements further away from the surface. The drawn contours indicate where integration was chosen to separate elements and obtain depth profiles as shown below.

Quantitative hydrogen, boron and carbon content

Time-of-Flight Elastic Recoil Detection (tof-ERD) was used, as XPS is generally not sensitive enough to provide a quantitative analysis of light elements such as boron and carbon, and cannot detect hydrogen. Furthermore, while XPS can extract information on depth distribution of elements, this is done by removing material from the top of the films using a sputter tool. This introduces sputter damage to the films and can redistribute elements in the films as not all elements are removed at the same rate (so-called preferential sputtering). As this phenomenon is especially relevant for light elements, the XPS depth profiles could be skewed from reality due to this effect. ERD typically does not impose sputter damage. While the depth resolution is typically not as good as XPS, the distribution of elements should be clear and unchanged by the measurement, providing a thorough sanity check to the XPS measurements. Figure 10 shows the ERD profile for the 1:20 sample. Boron is clearly present from the ^{10}B and ^{11}B profiles, according to their natural abundances (19.9 At% and 80.1 At%, respectively). Carbon can be seen throughout the sample, but at a very low level (<1 At%), explaining the lack of carbon detected by XPS. The data show the presence of hydrogen in the film, which could not be detected by XPS. As the masses of Al

1
2
3
4
5
6
7
8
9
10
11
12
13
14
15
16
17
18
19
20
21
22
23
24
25
26
27
28
29
30
31
32
33
34
35
36
37
38
39
40
41
42
43
44
45
46
47
48
49
50
51
52
53
54
55
56
57
58
59
60

and Si are very close, their so-called banana curves overlap, but a separation can be made based on the presence of isotopes for Si.

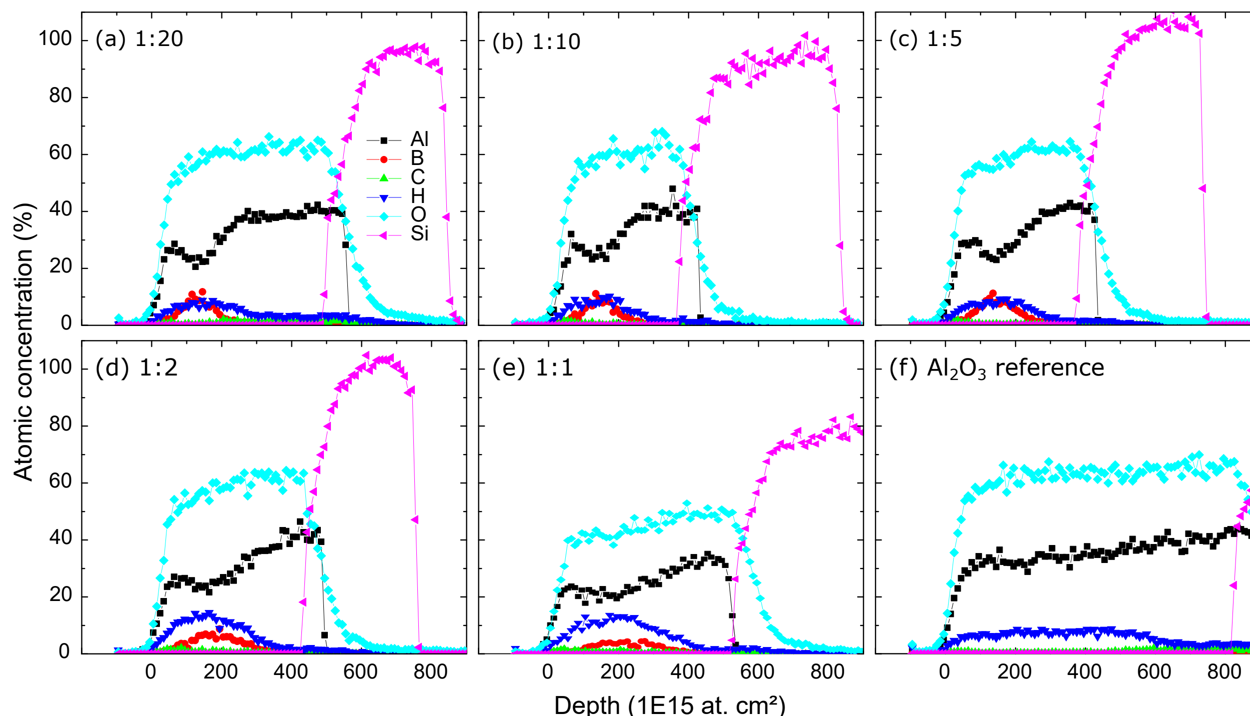

Figure 11: ERD depth profiles, extracted by analysing the spectra as in Figure 10 using the Potku software package. Elemental distributions of (a) 1:20, (b) 1:10, (c) 1:5, (d) 1:2, (e) 1:1 samples and (f) a reference Al_2O_3 sample deposited under the same conditions.

Figure 11 shows the extracted depth profiles, based on the analysis of recorded ERD spectra such as Figure 10. The boron distribution in the sample supports that measured in the XPS spectra, albeit at slightly lower concentrations. The B-concentration for the 1:20 sample peaks at around 10 At%, and that of the 1:1 sample around 5 At%. Interestingly, the boron distribution for the 1:1 sample appears to be rather constant throughout the film. From XPS however, all boron concentration profiles seem to be distributed according to a Gaussian distribution. Furthermore, the total boron concentration in the films is almost unaffected by the deposition condition in Figure 11(a) to (e), and is around $(12 \pm 2) \times 10^{15}$ at /cm^2. This is a surprising result, as the number of TMB-containing subcycles varies from 200 to 100 from the 1:20 to the 1:1 deposition condition. It appears that only the boron- and hydrogen

1
2
3
4
5
6
7
8
9
10
11
12
13
14
15
16
17
18
19
20
21
22
23
24
25
26
27
28
29
30
31
32
33
34
35
36
37
38
39
40
41
42
43
44
45
46
47
48
49
50
51
52
53
54
55
56
57
58
59
60

depth profiles are dependent on the number of TMB-containing subcycles, not the amount of boron incorporated into the films.

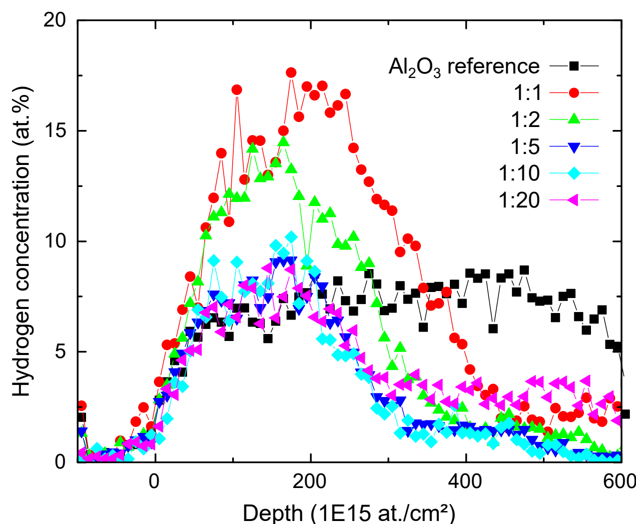

Figure 12: Detailed hydrogen distribution in the deposited films, as determined by ERD.

Furthermore, a significant amount of hydrogen is present in the films, as shown in Figure 12. Interestingly, the Al_2O_3 reference film in Figure 11(f) also contains about 7.5 At% hydrogen, resulting in about $(42 \pm 2) \times 10^{15}$ at /cm^2 in this film. The hydrogen is uniformly incorporated into most of the film, except for a region near the silicon substrate, where the hydrogen concentration drops to about 3.2 At% hydrogen. It is widely accepted that, even with plasma-enhanced ALD, fragments of precursor ligands are sometimes incorporated into ALD films, resulting in hydrogen incorporation, although this typically happens much more at low temperature, for example for TMA and water.[68] However, given the low carbon concentration found in these films, is seems more likely that the H-incorporation can be in the form of unreacted hydroxyl groups. The doped samples on the other hand do not contain a uniform distribution of hydrogen, but the hydrogen is concentrated at the region where the boron is also present as a dopant. In case of the 1:1-deposited sample, approximately the same amount of hydrogen is present as in the reference sample ($(49 \pm 2) \times 10^{15}$ at /cm^2), but concentrated around the middle of the deposited film (17 at %) with decreasing con-

1
2
3
4
5
6
7
8
9
10
11
12
13
14
15
16
17
18
19
20
21
22
23
24
25
26
27
28
29
30
31
32
33
34
35
36
37
38
39
40
41
42
43
44
45
46
47
48
49
50
51
52
53
54
55
56
57
58
59
60

centration towards the silicon interface. For higher TMB-containing subcycles, the total hydrogen content of the films actually decreases, down to about $(25 \pm 2) \times 10^{15}$ at /cm^2 for the 1:20 sample. In that case, all hydrogen is also again amassed around the boron-rich region near the surface, peaking at about 9 At% H. This also implies that there is a region below the boron-rich region and the Si substrate, i.e. between 300×10^{15} at /cm^2 and 500×10^{15} at /cm^2, that contains a lower hydrogen content (below 3 At%). For the 1:10 and 1:5 conditions, this 'cleaning' effect is even more pronounced, as the contain lower-region hydrogen contents below 1.5 At%, which is far cleaner compared to about 7.5 At% for the reference sample, and even compared to the 3 At% for the silicon interface region of the reference sample. In this way, applying TMB-containing subcycles can actually be used to control the H depth profile in the Al_2O_3 films. This could be useful for barrier layer applications or applications that require a high breakdown voltage (which will be influenced by impurities), or for deliberately doping a region with B and/or H in a stack of materials for applications in for example photovoltaics, where the hydrogen could play a role in passivating defects at Al_2O_3/SiO_2 interfaces.

Besides the peculiar elemental distributions, the thickness of the films was also far higher than expected from simple film growth by stacking nanolayers. According to the summed growth rates, these films should vary in thickness from 13 nm (1:20 sample) to 18 nm (1:1 sample), including a 5 nm Al_2O_3 capping layer. Fitting of the XRR data for the 1:20 and 1:10 samples reveals their total thickness to be 33 and 35 nm, respectively. Moreover, a multilayer model consistent with the XPS and ERD is required for a good fit. The fitted density values indicate that the bottom layer has a density of approximately 3.6 g cm^{-3}, typical of pure Al_2O_3 thin films. The boron-containing top layer is considerably less dense at 2.4 g cm^{-3} to 2.6 g cm^{-3}. The fitted roughness values are reasonably low at 2.5 – 3.5 nm. It was not possible to determine film thickness of the other samples due to the increasingly graded nature of the hydrogen and boron in these films. Ellipsometry was also

1 2 3 4 5 6 7 8 9 10 11 12 13 14 15 16 17 18 19 20 21 22 23 24 25 26 27 28 29 30 31 32 33 34 35 36 37 38 39 40 41 42 43 44 45 46 47 48 49 50 51 52 53 54 55 56 57 58 59 60

complicated by the complex compositional variation within the films. However the thickness of these films can be estimated from the XPS depth profiles. The capping layer is clearly present, and can be defined as the region up to which the boron concentration is rising, i.e. approximately 500 seconds sputtering time in Figure 9(a). As the boron only makes up a small fraction of the films, the sputter time will be almost equal in the pure Al_2O_3 films as in the B-doped regions, so the film thickness is linearly correlated to sputtering time. If we assume 500s is the capping layer, which is approximately 5 nm, the 1:20 film is approximately 35 nm thick, a close match to the XRR value. Using this approach, it is evident that the sample thicknesses increase with increasing TMA/O_2-plasma subcycles. The 1:1 film with largest fraction of TMA-containing subcycles can be estimated at approx. 50 nm rather than the predicted 18 nm. Indeed, cross-SEM measurements (not shown here) confirm this thickness estimation to be valid. This indicates that the typical assumption that only the surface of the deposited layer is reactive towards the next precursor exposures can no longer be valid, and the precursors (the TMA, in particular) in fact interact with the sub-surface/near-surface region of the already-deposited films, resulting in enhanced growth.

Understanding sub-surface reactions during the TMA pulse

The hypothesis of the sub-surface reactions is in line with the total amount of aluminum atoms detected in these films. Surprisingly, that number is comparable for all these samples (140 at /cm^2 to 180 at /cm^2). This is a surprising result given that the number of TMA-based cycles, including the cycles for the 5 nm Al_2O_3 capping layer, varies from 60 (for the 1:20 sample) to 150 (for the 1:1 sample). This implies that the amount of Al-atoms incorporated into the films from every TMA pulse is higher than it would be in a classical ALD process like the TMA-O_2 plasma process, as is shown in Figure 13. The value approaches that of the the reference Al_2O_3 films for the 1:1 samples, where most of the cycles are indeed already TMA-containing, as is clear from table 2.

ACS Paragon Plus Environment

1
2
3
4
5
6
7
8
9
10
11
12
13
14
15
16
17
18
19
20
21
22
23
24
25
26
27
28
29
30
31
32
33
34
35
36
37
38
39
40
41
42
43
44
45
46
47
48
49
50
51
52
53
54
55
56
57
58
59
60

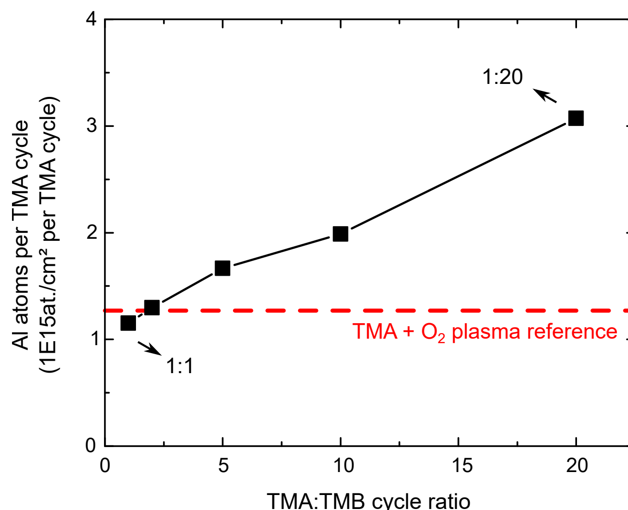

Figure 13: Total number of aluminium atoms grown into the total film, as extracted from the ERD depth profiles in Figure 10. The number of Al atoms is normalised to the number of TMA-containing ALD cycles used in the total process (see table 2), and plotted as a function of TMA to TMB cycle ratio.

To study this, in-situ FTIR and quasi-real-time in-situ ellipsometry were used during the intermixing and growth. First, the TMA and O_2 pulses were split into 10 sub-pulses of 2 seconds each. Spectroscopic ellipsometry was recorded after every sub-pulse, effectively determining saturation and optical thickness of the deposited layer. Figure 14(a) shows this on an already-grown ALD Al_2O_3 film. Essentially, the saturation behaviour of TMA and O_2 is observed. The major change in optical thickness of these films occurs during the first TMA and O_2 plasma pulses, corresponding to TMA chemisorption and ligand combustion. This indicates that two seconds of pulsing is sufficient for both TMA and O_2 plasma on this surface. The datapoints in Figure 14 are an average of 10 individual measurements, which indicate good reproducibility. Next, the same TMA-O_2 plasma pulsing was studied on a film grown by 20 alternating pulses of TMB and O_2 plasma, as described above. Figure 14(b) reveals that the growth on this surface is very different, in two aspects. Firstly, the first Al_2O_3 cycle on the TMB-O_2 plasma-grown surface reveals a higher TMA uptake compared to the same on the Al_2O_3 surface in Figure 14(a), and more 2s-pulses are needed before saturation is reached. This could potentially indicate that the TMA is not only chemisorbing

1
2
3
4
5
6
7
8
9
10
11
12
13
14
15
16
17
18
19
20
21
22
23
24
25
26
27
28
29
30
31
32
33
34
35
36
37
38
39
40
41
42
43
44
45
46
47
48
49
50
51
52
53
54
55
56
57
58
59
60

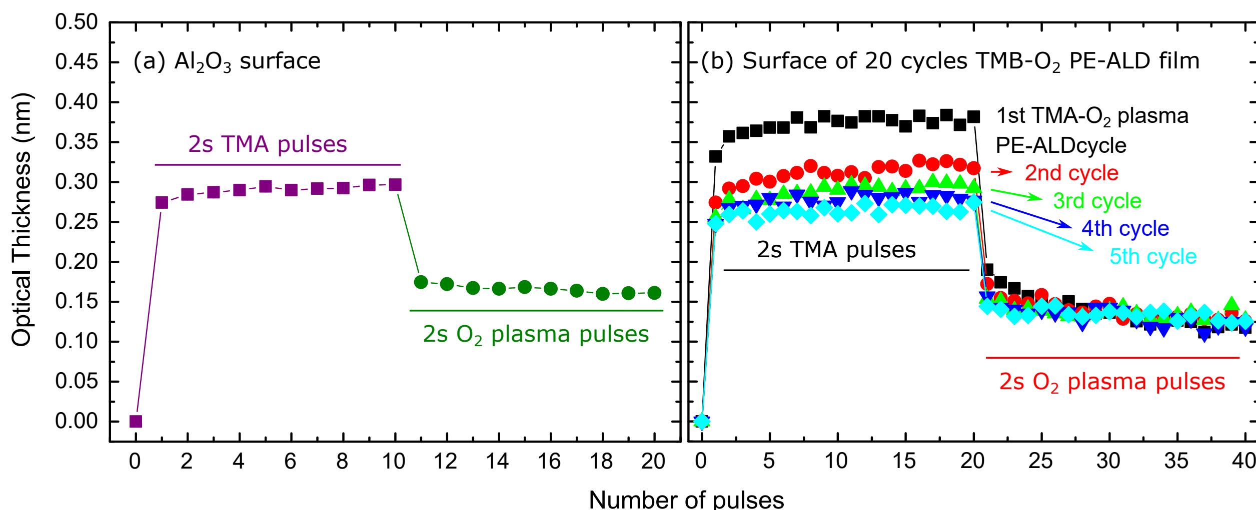

Figure 14: In-situ spectroscopic ellipsometry measurements during ALD using TMA and O_2 plasma. Every datapoint equals an average of 10 measurements. The error bars are omitted for clarity, but a standard deviation well below 0.01 nm was found. Subsequent TMA and O_2 plasma exposure to (a) an ALD-grown Al_2O_3 film and (b) a film grown with the TMB-O_2 plasma process described above. The optical thickness is obtained by fitting the collected data to an optical model for ALD Al_2O_3.

on the surface, but is also interacting with the underlying film in some way. However, the subsequent O_2 plasma pulses reduce this higher optical thickness back to a value close to that observed in Figure 14(a). Secondly, the subsequent TMA-O_2 plasma cycles no longer overlap with the initial cycle, indicatinsg that the surface is altered in a way that 'passivates' this anomalous behaviour, and returns the surface back to ALD Al_2O_3. This observation is supported by the fact that in XPS and ERD (Figures 9 and 11), the Al_2O_3 capping layer on the surface was indeed present. If the incorporation of TMB-O_2 plasma ALD cycles in the overall process would imply a permanently anomalous TMA-O_2 plasma ALD behaviour, this well-defined Al_2O_3 capping layer would not be expected.

In-situ FTIR recorded under the same process conditions is shown in Figure 15, and exhibits the same behaviour. TMA and O_2 plasma on the Al_2O_3 surface (Figure 15(a)) behaves as reported, with Al-OH groups being consumed, an Al-O stretching mode and a CH_3 deformation, originating from Al-CH_3, being introduced during the TMA pulses, and Al-OH

1
2
3
4
5
6
7
8
9
10
11
12
13
14
15
16
17
18
19
20
21
22
23
24
25
26
27
28
29
30
31
32
33
34
35
36
37
38
39
40
41
42
43
44
45
46
47
48
49
50
51
52
53
54
55
56
57
58
59
60

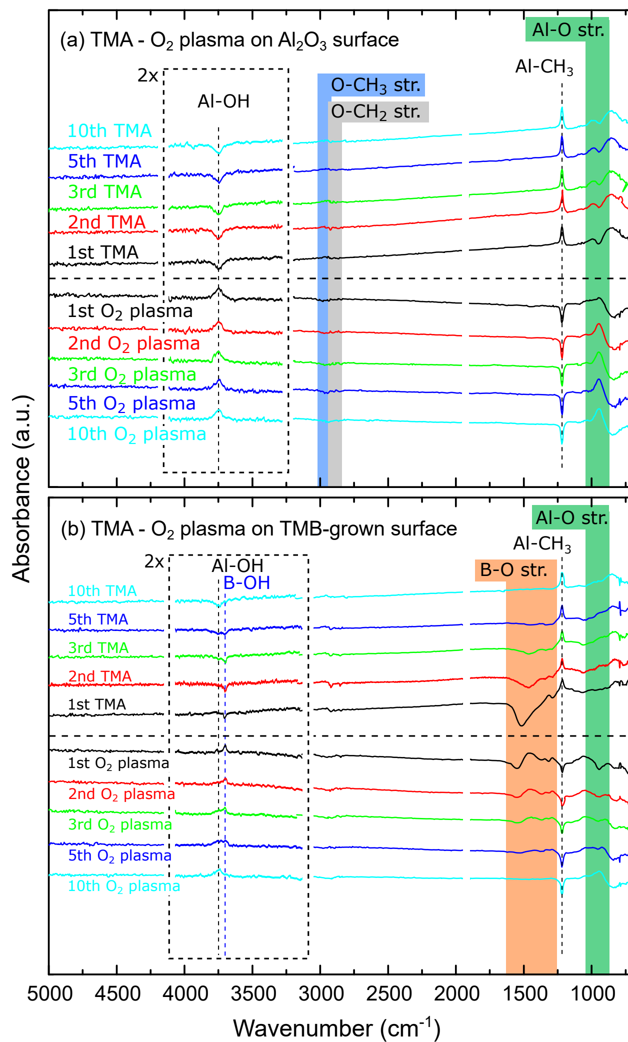

Figure 15: FTIR difference spectra between 680 cm^{-1} and 5000 cm^{-1} during ALD Al_2O_3 growth using TMA and O_2 plasma on (a) an ALD Al_2O_3 surface and (b) a film grown with the TMB-O_2 plasma process described above.

1
2
3
4
5
6
7
8
9
10
11
12
13
14
15
16
17
18
19
20
21
22
23
24
25
26
27
28
29
30
31
32
33
34
35
36
37
38
39
40
41
42
43
44
45
46
47
48
49
50
51
52
53
54
55
56
57
58
59
60

groups being re-created by combustion of the CH_3 ligands during the O_2 plasma pulse.[58–60,63] The same process on the TMB-O_2 PE-ALD films reveals a large interaction with the underlying films in the B-O region. This is further corroborated by the hydroxyl region: during the first cycles, B-OH surface groups are re-instated after the O_2 plasma pulse, while after 10 cycles only Al-OH groups are being formed. The 10th cycle in this case on Figure 15(b) is almost identical to the spectra in Figure 15(a). This indicated that, during the initial alumina cycles on the TMB-grown surface, the B-containing layer is altered by the TMA exposure, and rather then just a surface-inhibited reaction mechanism, some sub-surface interaction can also occur, until the surface is made sufficiently alumina-like. In this case, that state occurs at cycle 10, after which the surface chemistry is stabilised to alumina-on-alumina (cf. Figure 15(a)), explaining why capping can be performed. From Figure 15(b), it is clear that the TMA-O_2 plasma process on a TMB-grown surface, interact with the sub-surface region of the previously grown films during the TMA exposure (see Figure 15(b)).

Discussion on the doping mechanism

Based on the data presented above, it is obvious that the growth mechanism is not straightforward. While the present data does not allow for conclusive description, a likely scenario can be conceived. Given the anomalously high concentration of aluminium oxide in the samples in relation to the number of TMA pulses applied, it is obvious that subsurface reactions with the B_2O_3 layer must occur. It is known that ligand exchange between TMA and B_2O_3 resulting in the formation of Al_2O_3 and volatile $B(CH_3)_3$.[69] This is supported by the disappearance of the B-O absorption bands in Figure 15(b) upon the initial TMA exposure. Likewise, the absence of hydrogen would be consistent with this type of conversion reaction as hydroxyl groups are not involved. On the other hand hydrogen is associated with the boron depth profile. As stated earlier, it is likely that the surface chemistry of the TMB/O_2-plasma process involves the formation of H_3BO_3 and subsequent dehydrolyzation to B_2O_3.

This transformation is likely not instant, but proceeds through several borohydroxide intermediates.[70] For the samples with highest number of TMB/O_2-plasma cycles allows for more time for the dehydrolysis and therefore the highest alumina content. If the deposited boron layer has not completely dehydrolyzed before the next TMA pulse, a full conversion reaction does not occur and an aluminium borohydroxide -like layer is formed. With process optimization, this allows for an quasi-continuous tuning of the B-concentration in the top region of the films, with the H-concentration linked to it. Furthermore, the conversion reaction between B_2O_3 and TMA could be harnessed to deposit high quality hydrogen-free alumina layers if the residual boron-rich layer can subsequently be etched away.

Conclusions

Trimethyl borate was investigated in depth as ALD precursors for the deposition of boron oxide with oxygen plasma as a co-reactant. Initial growth was observed but a growth inhibition was found to occur after several cycles. It is revealed that the Lewis acidity of the available surface sites are DFT cluster calculations in combination with in-situ FTIR demonstrated that because of its weak Lewis acidity, the TMB molecule is found to adsorb via hydrogen-bonding to B-OH covered surfaces, without elimination of ligands. On the other hand, surface with sufficient Lewis basicity such as Al-OH, can facilitate the chemisorption of TMB. When the TMB-O_2 plasma was combined with intermediate TMA-O_2 plasma PE-ALD cycles, the growth was continuous with characteristics of surface saturation limited growth. However, rather than a uniformly Al-doped B_2O_3 film, the addition of these intermediate TMA-O_2 plasma PE-ALD cycles resulted in an Al_2O_3 film that was surface-region doped with boron and hydrogen, with the extent of this region mainly determined by the cycling ratios. A mechanism for this was proposed based on in-situ FTIR in combination with in-situ ellipsometry studies, and relies primarily on sub-surface interaction of the TMA

1
2
3
4
5
6
7
8
9
10
11
12
13
14
15
16
17
18
19
20
21
22
23
24
25
26
27
28
29
30
31
32
33
34
35
36
37
38
39
40
41
42
43
44
45
46
47
48
49
50
51
52
53
54
55
56
57
58
59
60

in the B-rich surface region, making this an interesting, albeit atypical, ALD process that allows for a quasi-analogue tuning of the B-concentration in the top region of high-purity Al_2O_3 films. It is evident that TMB, and perhaps other boron precursor, displays a rather complex surface chemistry that has big outcome on the film properties as well as on the general reproducibility of the results. Moreover, in regards to deposition of ternary materials with ALD using the subcycle approach, chemistries that are unsuited for binary processes, can still be applicable. In this, in-situ characterization methods and theoretical calculations are key elements in understanding the underlying mechanisms.

Supporting Information Available

DFT cluster calculation resulting structures and reaction energies ($kJ\,mol^{-1}$) computed with DFT at B3LYP / LAV3P** level for reactive adsorption sequence on $B(OH)_3$ and $Al(OH)_3$ surface models. Table S1: adsorption of TMB precursor onto hydroxylated surfaces (molecular adsorption of TMB via H-bonding, molecular adsorption of B(OMe)3 via H-bonding, elimination of MeOH from Lewis adduct). Table S2: adsorption of TEB precursor onto hydroxylated surfaces (molecular adsorption of TEB via H-bonding, rearrangement of H-bonding to Lewis adduct, elimination of EtOH from Lewis adduct). Table S3: Adsorption of TMA precursor onto hydroxylated surfaces (Adsorption of TMA as Lewis acid-base adduct, Elimination of CH_4 from Lewis adduct

Acknowledgement

The authors acknowledge FWO projects (grant number 1S68518N, GO87418N) for financial support. J. D. and M.M. acknowledge FWO-Vlaanderen for postdoctoral fellowships.

1 2 3 4 5 6 7 8 9 10 11 12 13 14 15 16 17 18 19 20 21 22 23 24 25 26 27 28 29 30 31 32 33 34 35 36 37 38 39 40 41 42 43 44 45 46 47 48 49 50 51 52 53 54 55 56 57 58 59 60

References

(1) Dean, C. R.; Young, A. F.; Meric, I.; Lee, C.; Wang, L.; Sorgenfrei, S.; Watanabe, K.; Taniguchi, T.; Kim, P.; Shepard, K. L.; Hone, J. Boron nitride substrates for high-quality graphene electronics. *Nature Nanotechnology* **2010**, *5*, 722–726.

(2) Park, H.; Kim, T. K.; Cho, S. W.; Jang, H. S.; Lee, S. I.; Choi, S.-Y. Large-scale synthesis of uniform hexagonal boron nitride films by plasma-enhanced atomic layer deposition. *Scientific Reports* **2017**, *7*, 40091.

(3) Sprenger, J. K.; Sun, H.; Cavanagh, A. S.; Roshko, A.; Blanchard, P. T.; George, S. M. Electron-Enhanced Atomic Layer Deposition of Boron Nitride Thin Films at Room Temperature and 100 °C. *The Journal of Physical Chemistry C* **2018**, *122*, 9455–9464.

(4) Berkemeier, F.; Shoar Abouzari, M. R.; Schmitz, G. Sputter-deposited network glasses: Structural and electrical properties. *Ionics* **2009**, *15*, 241–248.

(5) Kim, J. M.; Park, G. B.; Lee, K. C.; Park, H. Y.; Nam, S. C.; Song, S. W. Li–B–O–N electrolytes for all-solid-state thin film batteries. *Journal of Power Sources* **2009**, *189*, 211–216.

(6) Zhou, A.; Wang, W.; Liu, Q.; Wang, Y.; Yao, X.; Qing, F.; Li, E.; Yang, T.; Zhang, L.; Li, J. Stable, fast and high-energy-density LiCoO2 cathode at high operation voltage enabled by glassy B2O3 modification. *Journal of Power Sources* **2017**, *362*, 131–139.

(7) Nagasubramanian, A.; Yu, D. Y. W.; Hoster, H.; Srinivasan, M. Enhanced cycling stability of o-LiMnO2 cathode modified by lithium boron oxide coating for lithium-ion batteries. *Journal of Solid State Electrochemistry* **2014**, *18*, 1915–1922.

(8) Shannon, R. D.; Taylor, B. E.; English, A. D.; Berzins, T. New Li solid electrolytes. *Electrochimica Acta* **1977**, *22*, 783–796.

1
2
3
4
5
6
7
8
9
10
11
12
13
14
15
16
17
18
19
20
21
22
23
24
25
26
27
28
29
30
31
32
33
34
35
36
37
38
39
40
41
42
43
44
45
46
47
48
49
50
51
52
53
54
55
56
57
58
59
60

(9) Horopanitis, E. E.; Perentzis, G.; Beck, A.; Guczi, L.; Peto, G.; Papadimitriou, L. Correlation between structural and electrical properties of heavily lithiated boron oxide solid electrolytes. *Journal of Non-Crystalline Solids* **2008**, *354*, 374–379.

(10) Okumura, T.; Takeuchi, T.; Kobayashi, H. All-solid-state lithium-ion battery using Li2.2C0.8B0.2O3 electrolyte. *Solid State Ionics* **2016**, *288*, 248–252.

(11) Park, K.; Yu, B.-C.; Jung, J.-W.; Li, Y.; Zhou, W.; Gao, H.; Son, S.; Goodenough, J. B. Electrochemical Nature of the Cathode Interface for a Solid-State Lithium-Ion Battery: Interface between LiCoO2 and Garnet-Li7La3Zr2O12. *Chemistry of Materials* **2016**, *28*, 8051–8059.

(12) Kazyak, E.; Chen, K.-H.; Davis, A. L.; Yu, S.; Sanchez, A. J.; Lasso, J.; Bielinski, A. R.; Thompson, T.; Sakamoto, J.; Siegel, D. J.; Dasgupta, N. P. Atomic layer deposition and first principles modeling of glassy Li3BO3–Li2CO3 electrolytes for solid-state Li metal batteries. *J. Mater. Chem. A* **2018**, *6*, 19425–19437.

(13) Detavernier, C.; Dendooven, J.; Sree, S. P.; Ludwig, K. F.; Martens, J. A. Tailoring nanoporous materials by atomic layer deposition. *Chemical Society Reviews* **2011**, *40*, 5242–5253.

(14) Longrie, D.; Deduytsche, D.; Detavernier, C. Reactor concepts for atomic layer deposition on agitated particles: A review. *Journal of Vacuum Science & Technology A* **2014**, *32*, 010802.

(15) Miikkulainen, V.; Leskela, M.; Ritala, M.; Puurunen, R. L. Crystallinity of inorganic films grown by atomic layer deposition: Overview and general trends. *Journal of Applied Physics* **2013**, *113*, 021301–021301–101.

(16) George, S. M. Atomic Layer Deposition: An Overview. *Chemical Reviews* **2010**, *110*, 111–131.

(17) Mackus, A. J. M.; Schneider, J. R.; MacIsaac, C.; Baker, J. G.; Bent, S. F. Synthesis of Doped, Ternary, and Quaternary Materials by Atomic Layer Deposition: A Review. *Chemistry of Materials* **2019**, *31*, 1142–1183.

(18) Sang, B.; Yamada, A.; Konagai, M. Growth of boron-doped ZnO thin films by atomic layer deposition. *Solar Energy Materials and Solar Cells* **1997**, *49*, 19–26.

(19) Yamamoto, Y.; Saito, K.; Takahashi, K.; Konagai, M. Preparation of boron-doped ZnO thin films by photo-atomic layer deposition. *Solar Energy Materials and Solar Cells* **2001**, *65*, 125–132.

(20) Ferguson, J.; Weimer, A.; George, S. Atomic layer deposition of boron nitride using sequential exposures of BCl3 and NH3. *Thin Solid Films* **2002**, *413*, 16–25.

(21) Bjelkevig, C.; Mi, Z.; Xiao, J.; Dowben, P. A.; Wang, L.; Mei, W.-N.; Kelber, J. A. Electronic structure of a graphene/hexagonal-BN heterostructure grown on Ru(0001) by chemical vapor deposition and atomic layer deposition: extrinsically doped graphene. *Journal of Physics: Condensed Matter* **2010**, *22*, 302002.

(22) Driver, M. S.; Beatty, J. D.; Olanipekun, O.; Reid, K.; Rath, A.; Voyles, P. M.; Kelber, J. A. Atomic Layer Epitaxy of h-BN(0001) Multilayers on Co(0001) and Molecular Beam Epitaxy Growth of Graphene on h-BN(0001)/Co(0001). *Langmuir* **2016**, *32*, 2601–2607.

(23) Jones, J.; Beauclair, B.; Olanipekun, O.; Lightbourne, S.; Zhang, M.; Pollok, B.; Pilli, A.; Kelber, J. Atomic layer deposition of h-BN(0001) on RuO2(110)/Ru(0001). *Journal of Vacuum Science & Technology A: Vacuum, Surfaces, and Films* **2016**, *35*, 01B139.

(24) Mårlid, B.; Ottosson, M.; Pettersson, U.; Larsson, K.; Carlsson, J.-O. Atomic layer deposition of BN thin films. *Thin Solid Films* **2002**, *402*, 167–171.

1 2 3 4 5 6 7 8 9 10 11 12 13 14 15 16 17 18 19 20 21 22 23 24 25 26 27 28 29 30 31 32 33 34 35 36 37 38 39 40 41 42 43 44 45 46 47 48 49 50 51 52 53 54 55 56 57 58 59 60

(25) Olander, J.; Ottosson, L. M.; Heszler, P.; Carlsson, J.-O.; Larsson, K. M. E. Laser-Assisted Atomic Layer Deposition of Boron Nitride Thin Films. *Chemical Vapor Deposition* **2005**, *11*, 330–337.

(26) Weber, M.; Koonkaew, B.; Balme, S.; Utke, I.; Picaud, F.; Iatsunskyi, I.; Coy, E.; Miele, P.; Bechelany, M. Boron Nitride Nanoporous Membranes with High Surface Charge by Atomic Layer Deposition. *ACS Applied Materials & Interfaces* **2017**, *9*, 16669–16678.

(27) Weber, M.; Iatsunskyi, I.; Coy, E.; Miele, P.; Cornu, D.; Bechelany, M. Novel and Facile Route for the Synthesis of Tunable Boron Nitride Nanotubes Combining Atomic Layer Deposition and Annealing Processes for Water Purification. *Advanced Materials Interfaces* **2018**, 1800056.

(28) Putkonen, M.; Niinistö, L. Atomic layer deposition of B2O3 thin films at room temperature. *Thin Solid Films* **2006**, *514*, 145–149.

(29) Saly, M. J.; Munnik, F.; Baird, R. J.; Winter, C. H. Atomic Layer Deposition Growth of BaB2O4 Thin Films from an Exceptionally Thermally Stable Tris(pyrazolyl)borate-Based Precursor. *Chemistry of Materials* **2009**, *21*, 3742–3744.

(30) Saly, M. J.; Munnik, F.; Winter, C. H. Atomic layer deposition of CaB2O4 films using bis(tris(pyrazolyl)borate)calcium as a highly thermally stable boron and calcium source. **2010**, *20*, 9995–10000.

(31) Saly, M. J.; Munnik, F.; Winter, C. H. The Atomic Layer Deposition of SrB2O4 Films Using the Thermally Stable Precursor Bis(tris(pyrazolyl)borate)strontium. *Chemical Vapor Deposition* **2011**, *17*, 128–134.

(32) Li, W.-M.; Elers, K.; Kostamo, J.; Kaipio, S.; Huotari, H.; Soininen, M.; Soininen, P. J.; Tuominen, M.; Haukka, S.; Smith, S.; Besling, W. Deposition of WNxCy thin films by

ALCVD trade; method for diffusion barriers in metallization. Proceedings of the IEEE 2002 International Interconnect Technology Conference (Cat. No.02EX519). 2002; pp 191–193.

(33) Kim, S.-H.; Oh, S. S.; Kim, K.-B.; Kang, D.-H.; Li, W.-M.; Haukka, S.; Tuominen, M. Atomic-layer-deposited WNxCy thin films as diffusion barrier for copper metallization. *Applied Physics Letters* **2003**, *82*, 4486–4488.

(34) Kim, S.-H.; Oh, S. S.; Kim, H.-M.; Kang, D.-H.; Kim, K.-B.; Li, W.-M.; Haukka, S.; Tuominen, M. Characterization of Atomic Layer Deposited WN x C y Thin Film as a Diffusion Barrier for Copper Metallization. *Journal of The Electrochemical Society* **2004**, *151*, C272–C282.

(35) Kim, W.-H.; Oh, I.-K.; Kim, M.-K.; Maeng, W. J.; Lee, C.-W.; Lee, G.; Lansalot-Matras, C.; Noh, W.; Thompson, D.; Chu, D.; Kim, H. Atomic layer deposition of B2O3/SiO2 thin films and their application in an efficient diffusion doping process. *Journal of Materials Chemistry C* **2014**, *2*, 5805–5811.

(36) Kalkofen, B.; Mothukuru, V. M.; Lisker, M.; Burte, E. P. P-type Doping of Silicon Suitable for Structures with High Aspect Ratios by Using a Dopant Source of Boron Oxide Grown by Atomic Layer Deposition. *ECS Transactions* **2012**, *45*, 55–67.

(37) Kalkofen, B.; Amusan, A. A.; Lisker, M.; Burte, E. P. Application of atomic layer deposited dopant sources for ultra-shallow doping of silicon: Application of atomic layer deposited dopant sources for ultra-shallow doping of silicon. *physica status solidi (c)* **2014**, *11*, 41–45.

(38) Kalkofen, B.; Amusan, A. A.; Bukhari, M. S. K.; Garke, B.; Lisker, M.; Gargouri, H.; Burte, E. P. Use of B_2O_3 films grown by plasma-assisted atomic layer deposition for shallow boron doping in silicon. *Journal of Vacuum Science & Technology A: Vacuum, Surfaces, and Films* **2015**, *33*, 031512.

(39) Garcia-Alonso, D.; E. Potts, S.; Helvoirt, C. A. A. v.; A. Verheijen, M.; M. Kessels, W. M. Atomic layer deposition of B-doped ZnO using triisopropyl borate as the boron precursor and comparison with Al-doped ZnO. *Journal of Materials Chemistry C* **2015**, *3*, 3095–3107.

(40) Hao, W.; Marichy, C.; Journet, C.; Brioude, A. A Novel Two-Step Ammonia-Free Atomic Layer Deposition Approach for Boron Nitride. *ChemNanoMat* **2017**, *3*, 656–663.

(41) Mane, A. U.; Elam, J. W.; Goldberg, A.; Seidel, T. E.; Halls, M. D.; Current, M. I.; Despres, J.; Byl, O.; Tang, Y.; Sweeney, J. Atomic layer deposition of boron-containing films using B2F4. *Journal of Vacuum Science & Technology A* **2016**, *34*, 01A132.

(42) Christopher, P. M.; Shilman, A. Vapor pressures of trialkyl borates. *Journal of Chemical & Engineering Data* **1967**, *12*, 333–335.

(43) Yamamoto, Y.; Ikakura, H.; Ohgawara, S.; Furukawa, M. Comparison of Deposition Characteristics between Triethyl and Trimethyl Borates in an Atmospheric Pressure Chemical Vapor Deposition Equipment with Tetraethyl Orthosilicate and O3. *Japanese Journal of Applied Physics* **1999**, *38*, 5018.

(44) Xie, Q.; Jiang, Y.-L.; Detavernier, C.; Deduytsche, D.; Meirhaeghe, R. L. V.; Ru, G.-P.; Li, B.-Z.; Qu, X.-P. Atomic layer deposition of TiO2 from tetrakis-dimethyl-amido titanium or Ti isopropoxide precursors and H2O. *Journal of Applied Physics* **2007**, *102*, 083521.

(45) Musschoot, J.; Xie, Q.; Deduytsche, D.; Van den Berghe, S.; Van Meirhaeghe, R. L.; Detavernier, C. Atomic layer deposition of titanium nitride from TDMAT precursor. *Microelectronic Engineering* **2009**, *86*, 72–77.

(46) Dendooven, J.; Deduytsche, D.; Musschoot, J.; Vanmeirhaeghe, R. L.; Detavernier, C.

Conformality of Al2O3 and AlN Deposited by Plasma-Enhanced Atomic Layer Deposition. *Journal of The Electrochemical Society* **2010**, *157*, G111–G116.

(47) Laitinen, M.; Rossi, M.; Julin, J.; Sajavaara, T. Time-of-flight – Energy spectrometer for elemental depth profiling – Jyväskylä design. *Nuclear Instruments and Methods in Physics Research Section B: Beam Interactions with Materials and Atoms* **2014**, *337*, 55–61.

(48) Arstila, K.; Julin, J.; Laitinen, M. I.; Aalto, J.; Konu, T.; Kärkkäinen, S.; Rahkonen, S.; Raunio, M.; Itkonen, J.; Santanen, J. P.; Tuovinen, T.; Sajavaara, T. Potku – New analysis software for heavy ion elastic recoil detection analysis. *Nuclear Instruments and Methods in Physics Research Section B: Beam Interactions with Materials and Atoms* **2014**, *331*, 34–41.

(49) Widjaja, Y.; Musgrave, C. B. Quantum chemical study of the mechanism of aluminum oxide atomic layer deposition. *Applied Physics Letters* **2002**, *80*, 3304–3306.

(50) Elliott, S. D.; Greer, J. C. Simulating the atomic layer deposition of alumina from first principles. *Journal of Materials Chemistry* **2004**, *14*, 3246–3250.

(51) Bochevarov, A. D.; Harder, E.; Hughes, T. F.; Greenwood, J. R.; Braden, D. A.; Philipp, D. M.; Rinaldo, D.; Halls, M. D.; Zhang, J.; Friesner, R. A. Jaguar: A high-performance quantum chemistry software program with strengths in life and materials sciences. *International Journal of Quantum Chemistry* **2013**, *113*, 2110–2142.

(52) Becke, A. D. Perspective: Fifty years of density-functional theory in chemical physics. *The Journal of Chemical Physics* **2014**, *140*, 18A301.

(53) Stephens, P. J.; Devlin, F. J.; Chabalowski, C. F.; Frisch, M. J. Ab Initio Calculation of Vibrational Absorption and Circular Dichroism Spectra Using Density Functional Force Fields. *The Journal of Physical Chemistry* **1994**, *98*, 11623–11627.

(54) Grimme, S.; Antony, J.; Ehrlich, S.; Krieg, H. A consistent and accurate ab initio parametrization of density functional dispersion correction (DFT-D) for the 94 elements H-Pu. *The Journal of Chemical Physics* **2010**, *132*, 154104.

(55) Goerigk, L.; Grimme, S. A thorough benchmark of density functional methods for general main group thermochemistry, kinetics, and noncovalent interactions. *Physical Chemistry Chemical Physics* **2011**, *13*, 6670–6688.

(56) Hay, P. J.; Wadt, W. R. Ab initio effective core potentials for molecular calculations. Potentials for K to Au including the outermost core orbitals. *The Journal of Chemical Physics* **1985**, *82*, 299–310.

(57) Hay, P. J.; Wadt, W. R. Ab initio effective core potentials for molecular calculations. Potentials for the transition metal atoms Sc to Hg. *The Journal of Chemical Physics* **1985**, *82*, 270–283.

(58) Levrau, E.; Van de Kerckhove, K.; Devloo-Casier, K.; Pulinthanathu Sree, S.; Martens, J. A.; Detavernier, C.; Dendooven, J. In Situ IR Spectroscopic Investigation of Alumina ALD on Porous Silica Films: Thermal versus Plasma-Enhanced ALD. *J. Phys. Chem. C* **2014**, *118*, 29854–29859.

(59) Tsyganenko, A. A.; Filimonov, V. N. Infrared spectra of surface hydroxyl groups and crystalline structure of oxides. *Journal of Molecular Structure* **1973**, *19*, 579–589.

(60) Socrates, G. *Infrared and Raman Characteristic Group Frequencies: Tables and Charts*; John Wiley & Sons: West Sussex, UK, 2001.

(61) Liu, C.-H.; Chen, B.-H.; Lee, D.-J.; Ku, J.-R.; Tsau, F. Trimethyl Borate Regenerated from Spent Sodium Borohydride after Hydrogen Production. *Ind. Eng. Chem. Res.* **2010**, *49*, 9864–9869.

(62) Zydor, A.; Kessler, V. G.; Elliott, S. D. First principles simulation of reaction steps in the atomic layer deposition of titania: dependence of growth on Lewis acidity of titanocene precursor. *Physical Chemistry Chemical Physics* **2012**, *14*, 7954–7964.

(63) Elliott, S. D.; Scarel, G.; Wiemer, C.; Fanciulli, M.; Pavia, G. Ozone-Based Atomic Layer Deposition of Alumina from TMA: Growth, Morphology, and Reaction Mechanism. *Chemistry of Materials* **2006**, *18*, 3764–3773.

(64) Fomengia, G. N.; Nolan, M.; Elliott, S. D. First principles mechanistic study of self-limiting oxidative adsorption of remote oxygen plasma during the atomic layer deposition of alumina. *Physical Chemistry Chemical Physics* **2018**, *20*, 22783–22795.

(65) Gilson, T. R. Characterisation of ortho- and meta-boric acids in the vapour phase. *Journal of the Chemical Society, Dalton Transactions* **1991**, 2463–2466.

(66) Broadhead, P.; Newman, G. The vibrational spectra of orthoboric acid and its thermal decomposition products. *Journal of Molecular Structure* **1971**, *10*, 157–172.

(67) Puurunen, R. L. Correlation between the growth-per-cycle and the surface hydroxyl group concentration in the atomic layer deposition of aluminum oxide from trimethylaluminum and water. *Applied Surface Science* **2005**, *245*, 6–10.

(68) Groner, M. D.; Fabreguette, F. H.; Elam, J. W.; George, S. M. Low-Temperature Al_2O_3 Atomic Layer Deposition. *Chemistry of Materials* **2004**, *16*, 639–645.

(69) Perrine, J. C.; Keller, R. N. Boroxines. I. Alkyl Derivatives1. *Journal of the American Chemical Society* **1958**, *80*, 1823–1827.

(70) Aghili, S.; Panjepour, M.; Meratian, M. Kinetic analysis of formation of boron trioxide from thermal decomposition of boric acid under non-isothermal conditions. *Journal of Thermal Analysis and Calorimetry* **2017**, *131*, 2443–2455.

1
2
3
4

Graphical TOC Entry

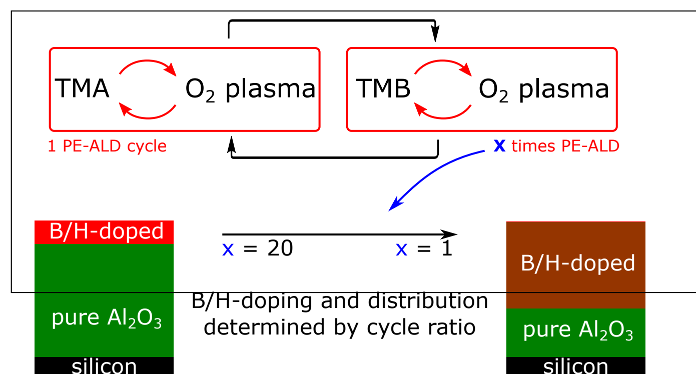

5
6
7
8
9
10
11
12
13
14
15
16
17
18
19
20
21
22
23
24
25
26
27
28
29
30
31
32
33
34
35
36
37
38
39
40
41
42
43
44
45
46
47
48
49
50
51
52
53
54
55
56
57
58
59
60